A Geometry-Based Multiple Bounce Model for Visible Light Communication Channels

(Invited Paper)

Ahmed Al-Kinani[1], Cheng-Xiang Wang[1], Harald Haas[2], and Yang Yang[3]

[1]Institute of Sensors, Signals and Systems, School of Engineering & Physical Sciences, Heriot-Watt University, Edinburgh EH14 4AS, UK.
[2]Institute of Digital Communications, School of Engineering, The University of Edinburgh, Edinburgh EH9 3JL, UK.
[3]Key Lab of Wireless Sensor Network and Communication, SIMIT, Chinese Academy of Sciences, Shanghai 200050, China.
Email: {aa1304, cheng-xiang.wang}@hw.ac.uk, h.haas@ed.ac.uk, yang.yang@mail.sim.ac.cn

Abstract—**High performance of visible light communication (VLC) systems requires overcoming the limitations imposed by the optical wireless channel distortions resulting from path loss and temporal dispersion. In order to design techniques to combat the effects of channel distortions, an accurate VLC channel model is needed. In this paper, we propose a new regular-shaped geometry-based multiple bounce model (RS-GBMB) for VLC channels. The proposed model employs a combined two-ring model and ellipse model, where the received signal is constructed as a sum of the line-of-sight (LoS), single-, double-, and triple bounced rays of different powers. This makes the model sufficiently generic and adaptable to a variety of indoor scenarios. Based on the proposed RS-GBMB model, statistical properties are then investigated, such as the channel DC gain, mean excess delay, root mean square (RMS) delay spread, and Rician factor.**

Keywords – **Visible light communications, channel modeling, channel DC gain, RMS delay spread, Rician factor.**

I. INTRODUCTION

Recently, VLC systems attracted ever increasing attention, particularly for indoor wireless data transmissions. They become a potential solution for mitigating the looming radio frequency (RF) spectrum crisis. Possessing the ability to provide illumination and wireless broadband communication simultaneously, VLC, has been identified as one of the robust solutions towards networked indoor wireless communication systems [1]. Based on the VLC idea, light fidelity (Li-Fi) terminology is introduced by [2]. VLC offers many ecological, security and economic features compared with RF such as environment-friendly, no health concerns, inherent security due to spatial confinement, an energy-efficient, low-cost technology [1] and higher area spectral efficiency (ASE) [3]. The vision is that VLC wireless networks would complement existing heterogeneous RF wireless networks to provide ubiquitous coverage. Furthermore, VLC seems in some aspects superior to Wi-Fi, infrared (IR), Bluetooth, and ZigBee for short-range communications, i.e., 1–10 m [3]. VLC systems utilize commercially available off-the-shelf incoherent white light emitting diodes (WLEDs) as optical signal transmitters (Tx). While high sensitive photodiodes (PDs) such as avalanche PDs (APDs) or single-photon avalanche diode (SPAD) are used as optical signal receivers (Rx). As the modulation of the phase or frequency of the incoherent light is difficult [4], information is modulated onto the intensity of the optical carrier, while the most practical down-conversion technique is the direct detection (DD). Intensity modulation with direct detection (IM/DD) has been considered as the de-facto modulation scheme for VLC due to its reduced cost and complexity [5].

Indoor channel characteristics depend upon the type of environment (residential or office buildings, factories, shopping malls, etc.), the scatterers and the positions of the Tx and Rx. Different optical-propagation environment would cause different optical channel characteristics. There have been a plentiful amount of work done on the channel characterization in the IR spectrum, e.g., [6] – [8]. However, visible light (VL) and IR bands exhibit different characteristics, which necessitates the development of VLC channel models to fill the research gaps. In [9], [10] the authors investigated VLC channels using deterministic ray tracing approach based on Zemax ®. In this paper, we derive a novel RS-GBMB model for VLC channel. In this model, the effective scatterers are located on regular shapes, i.e., two-ring and ellipse. RS-GBMB model is able to model the following channel components

1) The LoS component
2) The single-bounced (SB) rays generated from the effective scatterers located on either of the two rings or the ellipse.
3) The double-bounced (DB) rays produced from the effective scatterers located on both two rings and/or the ellipse.
4) The triple-bounced (TB) rays produced from the effective scatterers located on both two rings and the ellipse.

RS-GBMB is mathematically tractable and to the best of the authors' knowledge, this is the first time that a RS-GBMB model is proposed to model VLC channels.

The rest of this paper is organized as follows. Section II describes VLC propagation scenario. Section III introduces the new VLC channel model. In section IV, VLC channel coefficient is derived. In Section V, simulation results and discussion are presented. Conclusions are finally drawn in Section VI.

31

Fig. 1. VLC Propagation scenario.

Fig. 2. Channel coefficient generation procedure.

II. VLC PROPAGATION SCENARIO

A basic VLC link configuration can be defined as a LoS and non-LoS (NLoS) which are both considered in this study. Six link configurations for optical wireless communications (OWC) and the trade-off between them are detailed in [7]. The proposed VLC propagation scenario is illustrated in Fig.1. The scenario is a meeting room designed using DIALux$^{®}$ [11]; a commercially available professional light planning software. Incoherent WLED lamps usually consist of a significant number of single chips, each presenting a generalized Lambertian radiation pattern can be expressed as [6]

$$R\left(\phi_T\right) = \frac{\alpha+1}{2\pi}\cos^\alpha\left(\phi_T\right) \qquad \phi_T \in [-\pi/2, \pi/2]. \quad (1)$$

Here, ϕ_T is the angle of irradiance which is commonly denoted as the angle of departure (AoD) and α is mode number of the radiation lobe, which specifies the directionality of the source. At the receiver, the PD is modelled as an active area A_R collecting the radiation incident at angle ϕ_R smaller than the PD's field of view (FoV). Only rays that incident within receiver's FoV will be captured. Angle ϕ_R is denoted as the angle of arrival (AoA). The wireless optical channel gain is proportional to the square of the distance between the Tx and Rx (the inverse square law), and to the effective collection area of the PD $A_{R_{eff}}$, which is given as [6]

$$A_{R_{eff}} = \begin{cases} A_R \cos(\phi_R) & 0 \le \phi_R \le \text{FoV} \\ 0 & \phi_R > \text{FoV}. \end{cases} \quad (2)$$

The PD can be integrated with end user device such as laptops, tablets, or smart phones as shown in Fig. 1.

III. VLC CHANNEL MODEL

The general procedure of channel fading coefficient or channel impulse response (CIR) generation can be depicted in Fig. 2. In this section, we describe the proposed VLC channel model. Let us now consider a general narrowband optical wireless system where the transmitter is WLED lamp which acts as fixed base station while the receiver is a PD acts as end user device. Fig. 3 illustrates the geometry of the proposed RS-GBMB model, which is a combination of a single-and double-bounce two-ring model, a single bounce ellipse model, a triple-bounce two-ring- ellipse model, in addition to the LoS
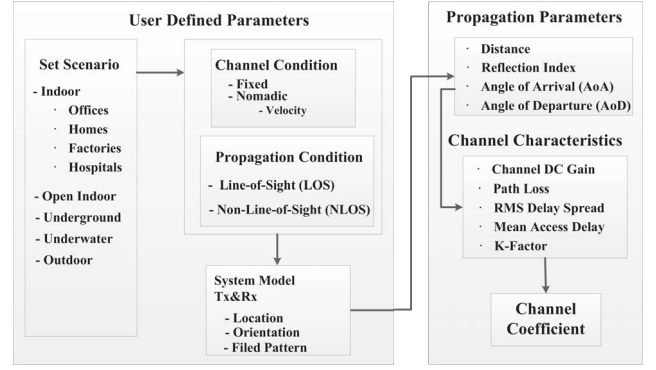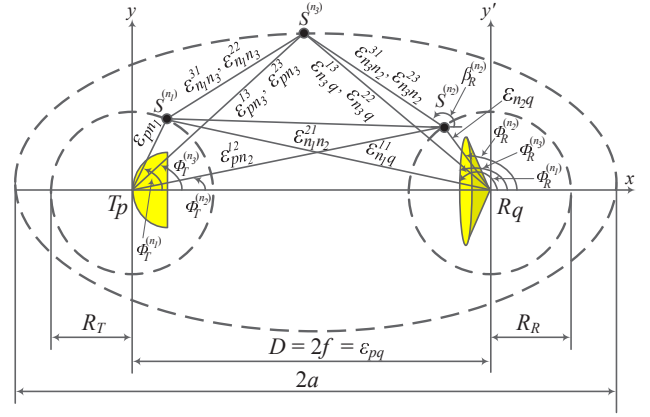

Fig. 3. A generic RS-GBMB indoor VLC channel model combining a two-ring model and an ellipse model.

component. The definitions of key geometry parameters are presented in Table I.

The two-ring scenario is proposed to model the scatterers around the Tx and Rx while the ellipse scenario is proposed to model the walls within indoor environments. Suppose there are N_1 local scatterers around the Tx lying on a ring of radius R_T and the n_1th ($n_1 = 1, ..., N_1$) local scatterer is denoted by S^{n_1}. Similarly, assume there are N_2 local scatterers around the Rx lying on a ring of radius R_R and the n_2th ($n_2 = 1, ..., N_2$) local scatterer is denoted by S^{n_2}. For the ellipse model, N_3 local scatterers lying on an ellipse and the n_3th ($n_3 = 1, ..., N_3$) local scatterer is denoted by S^{n_3}. Ellipses are confocal, i.e., they have common focal points (foci), which in our case coincide with the position of the Tx and Rx. The ellipse parameters a and b are denoting the semi-major axis and semi-minor axis, respectively. The distance between the Tx and Rx is $D = 2f$ and the equality $a^2 = b^2 + f^2$ holds.

IV. VLC CHANNEL COEFFICIENT

The proposed channel model expresses CIR between the Tx and the Rx as the superposition of the LoS and the higher-

TABLE I: Definitions of key geometry parameters.

Component	Optical Path	Distance
LoS	$T_p \rightarrow R_q$	ε_{pq}
1- SB_11	1- $T_p \rightarrow n_1 \rightarrow R_q$	1- $\varepsilon_{pn_1} + \varepsilon_{n_1 q}^{11}$
2- SB_12	2- $T_p \rightarrow n_2 \rightarrow R_q$	2- $\varepsilon_{pn_2}^{12} + \varepsilon_{n_2 q}$
3- SB_13	3- $T_p \rightarrow n_3 \rightarrow R_q$	3- $\varepsilon_{pn_3}^{13} + \varepsilon_{n_3 q}^{13}$
1- DB_21	1- $T_p \rightarrow n_1 \rightarrow n_2 \rightarrow R_q$	1- $\varepsilon_{pn_1} + \varepsilon_{n_1 n_2}^{21} + \varepsilon_{n_2 q}$
2- DB_22	2- $T_p \rightarrow n_1 \rightarrow n_3 \rightarrow R_q$	2- $\varepsilon_{pn_1} + \varepsilon_{n_1 n_3}^{22} + \varepsilon_{n_3 q}^{22}$
3- DB_23	3- $T_p \rightarrow n_3 \rightarrow n_2 \rightarrow R_q$	3- $\varepsilon_{pn_3}^{23} + \varepsilon_{n_3 n_2}^{23} + \varepsilon_{n_2 q}$
1- TB_31	$T_p \rightarrow n_1 \rightarrow n_3 \rightarrow n_2 \rightarrow R_q$	$\varepsilon_{pn_1} + \varepsilon_{n_1 n_3}^{31} + \varepsilon_{n_3 n_2}^{31} + \varepsilon_{n_2 q}$

order components reflected off the local scatterers as [12]

$$h_{pq}(t) = h_{pq}^{\text{LoS}}(t) + \sum_{i=1}^{I} \sum_{g=1}^{f_I(i)} h_{pq}^{ig}(t) \quad (3)$$

where $(I \geq 1)$ is the number of related local scattering areas, $f_I(i) = \frac{I!}{(I-i)! \times i!}$ denotes the total possible number of bonuses based on the number of local scattering areas, and $h_{pq}^{ig}(t)$ represents the CIR of the gth scattered component consisting of i-bounced rays. For example, $h_{pq}^{31}(t)$ denotes the first triple-bounced component. For the wireless optical communication environment shown in Fig. 1 with I= 3, the proposed model framework consists of the LoS component, $f_3(1)$= 3 single-bounced components, $f_3(2)$= 3 double-bounced components, $f_3(3)$= 1 triple-bounced components. The complexity in calculating the CIR grows as higher order reflections are considered. On the other hand the contribution of the higher order reflections to the overall impulse response is significantly declining since $\|h_{pq}^{\text{NLoS}}\| \rightarrow 0$, $i \rightarrow \infty$. It has been proved that the reflected power from the third bounce is very small, which is less than 5% in most link configurations [8]. Therefore, we will consider the CIR for only primary reflections (up to 3), and, hence (3) can be re-written as

$$h_{pq}(t) = h_{pq}^{\text{LoS}}(t) + h_{pq}^{\text{SB}}(t) + h_{pq}^{\text{DB}}(t) + h_{pq}^{\text{TB}}(t). \quad (4)$$

In order to make the proposed model more practical, we assumed the following two practical criteria: firstly, the $i-\text{th}$ bounced rays are always bounced by S^{n_i} ($i \in \{1, 2, 3\}$) scatterers located in different local scattering areas from far to near relative to the receiver [13]. Secondly, excluding the scatterers behind Tx and out of Rx FoV. Based on these practical criteria, some i-bounced components are not necessarily to be considered.

A. The LoS Link ($h_{pq}^{\text{LoS}}(t)$)

In the proposed model, the CIR of the LoS component is deterministic and given as [7]

$$h_{pq}^{\text{LoS}}(t) = \frac{A_R}{\pi(\varepsilon_{pq})^2} \cos^{\alpha}(\phi_T) \cos(\phi_R) \delta(t - \frac{\varepsilon_{pq}}{c}). \quad (5)$$

B. Single-Bounce Link ($h_{pq}^{\text{SB}}(t)$)

In general, for NLoS configration, each scatterer $S^{(n_i)}$ introduces a gain $G^{(n_i)}$. This parameter is dependent on the surface reflection coefficient $\rho(\lambda)$ of the scatterer $S^{(n_i)}$. Hence, the channel gain of a specific path $T_p - S^{(n_i)} - R_q$, caused by the nth transmitted plane wave from Tx, interacting with the local scatterer $S^{(n_i)}$ and then arriving at the Rx, can be written as

$$h_{T_p - S^{(n_i)} - R_q}^{\text{NLoS}}(t) = \sum_{i=1}^{3} \sum_{n=1}^{N} \frac{G^{(n_i)} A_R}{\pi(D_{pq})^2} \cos(\phi_T^n)^{\alpha}$$
$$\times \cos(\phi_R^n) \, \delta(t - \frac{D_{pq}}{c}). \quad (6)$$

Here, D_{pq} represents the total distance through different paths between the Tx and Rx.

1) Single-Bounce in Two-Ring Model ($h_{pq}^{11}(t)$ and $h_{pq}^{12}(t)$): The first probable optical path within single-bounce model is through the link $T_p - n_1 - R_q$. We assume an isotropic scattering along Tx-Ring characterized by a uniform distribution of the AoD ϕ_T, i.e.,

$$\text{P}(\phi_T) = \frac{1}{\pi} \quad , \quad \phi_T \in [-\pi/2, \pi/2]. \quad (7)$$

Accordingly, the distance $\varepsilon_{n_1 q}^{11}$ can be calculated by using the law of cosine in triangle $T_p - n_1 - R_q$ as

$$\varepsilon_{n_1 q}^{11} = \sqrt{(R_T)^2 + (D)^2 - 2R_T D \cos(\phi_T)}. \quad (8)$$

The relationship between the AoD ϕ_T and corresponding AoA ϕ_R can be found by using law of sines in the triangle $T_p - n_1 - R_q$ as follows:

$$\phi_R = \sin^{-1}[\frac{R_T \sin(\phi_T)}{\sqrt{(R_T)^2 + (D)^2 - 2R_T D \cos(\phi_T)}}]. \quad (9)$$

Once AoA and AoD are determined as above, with the total distance of link $T_p - n_1 - R_q$ given in Table I, $h_{pq}^{11}(t)$ can be determined using (6). The second probable optical path within two-ring model will be through the link $T_p - n_2 - R_q$. In this case we have followed the procedure above to calculate $\varepsilon_{pn_2}^{12}$, AoD ϕ_T, scatterers coordinates along the Rx-Ring and $h_{pq}^{12}(t)$.

2) Single-Bounce in Ellipse Model ($h_{pq}^{13}(t)$): The last probable optical path will be within ellipse model through the link $T_p - n_3 - R_q$. The single-bounce ellipse model can be derived based on pure ellipse properties mentioned above. The same assumption above ($\phi_R \curvearrowright U(0, 1/\text{FoV}), \phi_R \in [0, \text{FoV}]$) can be used in ellipse model. The total optical path of the link $(T_p - n_3 - R_q)$ is $\varepsilon_{pn_3}^{13} + \varepsilon_{n_3 q}^{13} = \varepsilon_{pq}^{13} = 2a$. According to law of cosines in triangle $T_p - n_3 - R_q$, the path length between the focal point and a specific scatterer is given as

$$\varepsilon_{pn_3}^{13} = \sqrt{(\varepsilon_{n_3 q}^{13})^2 + (2f)^2 - 2(\varepsilon_{n_3 q}^{13})(2f) \cos(\phi_R)}. \quad (10)$$

Based on ellipse properties and after some manipulation, we can get the path length as a function of AoA

$$\varepsilon_{pn_3}^{13} = \frac{a^2 + f^2 - 2af \cos(\phi_R)}{a - f \cos(\phi_R)}. \quad (11)$$

Substituting (11) to (10), we get

$$\varepsilon_{n_3 q}^{13} = \frac{b^2}{a - f \cos(\phi_R)}. \quad (12)$$

Applying the laws of sines to the triangle $T_p - n_3 - R_q$ in order to find the relationship between the AoA and AoD for ellipse scattering region, we get

$$\phi_T = \sin^{-1}\left[\frac{b^2\cos(\phi_R)}{a^2 + f^2 + 2af\cos(\phi_R)}\right].\qquad(13)$$

Now, $(h_{pq}^{13}(t))$ can be determined by substituting AoA, AoD and path length $2a$ in (6). Once the path lengths between the Tx and the Rx via a scatterer along the ellipse $\varepsilon_{pn_3}^{13}$ and $\varepsilon_{n_3q}^{13}$ are calculated, the scatterers coordinates can be determined either through $x_{n_3} = \varepsilon_{n_3q}^{13}\cos(\phi_R), y_{n_3} = \varepsilon_{n_3q}^{13}\sin(\phi_R)$, or by using intersection between the focal points and the ellipse.

C. Double-Bounce Link $(h_{pq}^{\mathrm{DB}}(t))$

1) Double-Bounce in Two-Ring Model (h_{pq}^{21}): In the case of the double-bounce two-ring model, both AoA and AoD are generated randomly as in sections IV-B. Each optical ray leaves the Tx with specific AoD will collide firstly one of the scatterers of Tx-Ring. Secondly, the scattered secondary rays will strike another scatterer on Rx-Ring and then collide the Rx with random AoA. The optical path length is taken by each ray can be calculated geometrically based on the scatterers coordinates along both rings. The scatterers coordinates along the Tx-Ring are $x_{n_1} = R\cos(\phi_T), y_{n_1} = R\sin(\phi_T)$, while the scatterer coordinates along the Rx-Ring are $x_{n_2} = D - R\cos(\phi_R), y_{n_2} = R\sin(\phi_R)$. Since the Tx and Rx coordinates are given, the optical path length can be obtained simply by applying Pythagoras theorem for above points, hence determine $(h_{pq}^{21}(t))$ components.

2) Double- Bounce in Two- Ring- Ellipse Model $(h_{pq}^{22}(t)$ and $h_{pq}^{23}(t))$: Before going further in determining other path lengths, it is worth to mention that there are equal distances shared between SB and DB ($\varepsilon_{pn_3}^{13}= \varepsilon_{pn_3}^{23}$, $\varepsilon_{n_3q}^{13}= \varepsilon_{n_3q}^{22}$). Likewise, there are equal distances shared between DB and TB ($\varepsilon_{n_1n_3}^{22}= \varepsilon_{n_1n_3}^{31}$, $\varepsilon_{n_3n_2}^{22}= \varepsilon_{n_3n_2}^{31}$).

The path lengths $\varepsilon_{n_1n_3}^{22}$ and $\varepsilon_{n_3n_2}^{23}$ for double-bounce (or $\varepsilon_{n_1n_3}^{31}$ and $\varepsilon_{n_3n_2}^{31}$ for triple-bounce) can be determined by using the method of intersection between ellipse and line. By using this method, we can assume that the incident/reflected rays can be represented by lines intercepted at scatterer S^{n_3} (or $x_{1_{n_3}}, y_{1_{n_3}}$).

According to the ellipse formula, if the center of ellipse is moved by $x = h$ and $y = k$, the ellipse equation can be written as [14]

$$\frac{(x-h)^2}{a^2} + \frac{(y-k)^2}{b^2} = 1\ ,\ \ a > b.\qquad(14)$$

Slope-Intercept form of the line is given by

$$y = mx + c\qquad(15)$$

Here, m and c are the slope of the line and y-axis intercept respectively. The intersection points are given by

$$x_{(1,2)_{n_3}} = \frac{hb^2 - ma^2\varepsilon \pm ab\sqrt{a^2m^2 + b^2 - \delta^2 - k^2 + 2\delta k}}{a^2m^2 + b^2}\qquad(16)$$

$$y_{(1,2)_{n_3}} = \frac{b^2\delta + ka^2m^2 \pm abm\sqrt{a^2m^2 + b^2 - \delta^2 - k^2 + 2\delta k}}{a^2m^2 + b^2}.\qquad(17)$$

Here, $\varepsilon = c - k$ and $\delta = c + mh$. The key assumption is that the scatterer point (x_{n_2}, y_{n_2}) at Rx-Ring should satisfy the equation of any line pass through that point and hence,

$$y_{n_2} = x_{n_2}m + c\qquad(18)$$

where $x_{n_2} = R_R\cos(\phi_R)$, $y_{n_2} = R_R\sin(\phi_R)$. In order to create a relation between two-ring and ellipse scattering regions for double and triple bounces, we introduced one more parameter , i.e., the angle of scattering (AoS) off Rx-Ring and it is denoted by β_R. Note that the AoD ϕ_T , AoS β_R and AoA ϕ_R are independent for double-bounced and triple- bounced rays, while AoD ϕ_T and AoA ϕ_R are interdependent for single-bounced rays. The angle β_R can be generated randomly and the slop in (18) is computed by

$$m = -\tan(\beta_R),\qquad(19)$$

while the y-axis intercept coordinate is

$$c = y_{n_2} - x_{n_2}m.\qquad(20)$$

The coordinates of above line can be obtained by substituting above coordinates and equations (19) and (20), in (15) to get

$$y = x\tan(\beta_R) + [R_R\sin(\phi_R) - (\tan(\beta_R)R_R\cos(\phi_R) + f)].\qquad(21)$$

Based on above assumption, the path length $\varepsilon_{n_3n_2}^{23}$ (or $\varepsilon_{n_3n_2}^{31}$) can be written as

$$\varepsilon_{n_3n_2}^{31} = \sqrt{(x_{1_{n_3}} - x_{n_2})^2 + (y_{1_{n_3}} - y_{n_2})^2}.\qquad(22)$$

The path length $\varepsilon_{n_1n_3}^{22}$ (or $\varepsilon_{n_1n_3}^{31}$) can be obtained as

$$\varepsilon_{n_1n_3}^{31} = \sqrt{(x_{1_{n_3}} - x_{n_1})^2 + (y_{1_{n_3}} - y_{n_1})^2}.\qquad(23)$$

It can be noticed from (22) and (23) that only $(x_{1_{n_3}}, y_{1_{n_3}})$ is considered, while $(x_{2_{n_3}}, y_{2_{n_3}})$ have been ignored.

D. Triple-Bounce Link $(h_{pq}^{\mathrm{TB}}(t))$

Although the triple-bounce scattered components $(h_{pq}^{31}(t))$ are less probable to be captured by the photodiode, they are contributing to the total scattered power. Furthermore, the effect of above second criterion can be significant. In this case, each optical ray leaves the Tx with specific AoD, will collide with, firstly one of the scatterers of Tx-Ring. Secondly, the scattered secondary ray will strike another scatterer on surrounded ellipse and thirdly, will collide with a scatterer on Rx-Ring and then captured by the Rx with random AoA within Rx FoV. Based on (3) and first criterion, the triple-bounce link bath is $T_p - n_1 - n_3 - n_2 - R_q$. By following the same assumption above for the AoA, and using the method of intersection between ellipse and line twice, we can determine $\varepsilon_{n_1n_3}^{31}$, $\varepsilon_{n_3n_2}^{31}$, and $(h_{pq}^{31}(t))$.

V. RESULTS AND DISCUSSIONS

In performing simulations, the entries of the environmental parameters are summarized in Table II.

TABLE II: Model Parameters used in computer simulations.

Model Parameters	
semi-major a & semi-minor b axes	3 m, 1.5 m
Walls (Brick Painted White)	$\rho_{\text{wall}}(\lambda) = 0.81$
Scaterers	$\rho_{\text{scaterer}}(\lambda) = 0.6$
Optical Source Parameters	
Type	LG F3630TC1N5B
Mode Number (α)	1
Photodiode Parameters	
Area	1 cm^2
Field of view (FoV)	80°
Other Parameters	
Number of Scaterers	40
Ring Radius (R_T, R_R)	1 m

A. VLC Channel Characteristics

1) VLC CIR : The resulting VLC CIR of $h_{pq}^{\text{LoS}}(t)$ and $h_{pq}^{\text{SB}}(t)$ components are shown in Fig. 4. While, $h_{pq}^{\text{DB}}(t)$ components are illustrated in Fig. 5. In Fig. 6, $h_{pq}^{\text{TB}}(t)$ is presented and finally, combined CIR of SB, DB and TB is shown in Fig. 7. Based on the obtained CIR, we further quantify fundamental channel characteristics as detailed in the next subsections.

2) Channel DC gain $H(0)$: It is one of the most important features of a VLC channels, as it determines the achievable signal-to-noise ratio (SNR) [9]. $H(0)$ is given as [5]

$$H(0) = \int_{-\infty}^{\infty} h(t)dt. \tag{24}$$

$H(0)$ is related to the average received power P_r, by $P_r = P_T H(0)$, where P_T is the average transmitted power. It will be convenient to compare results under the assumption that the transmitted power is 1 W.

3) Delay Spread: Due to the difference in propagation length of the various optical paths, the received signal is dispersed over time. This will induce multipath temporal dispersion at receiving side. Temporal dispersion can be quantified by the channel RMS delay spread σ_τ [5]

$$\sigma_\tau = \sqrt{\frac{\sum_i (\tau_i - \mu_\tau)^2 h_i^2(t)}{\sum_i h_i^2(t)}} \tag{25}$$

where μ_τ is the mean excess delay: $\mu_\tau = \frac{\sum_i \tau_i \, h_i^2(t)}{\sum_i h_i^2(t)}$. RMS delay spread is critical in high-speed applications, where the maximum bit rate $R_b \leq 1/10\sigma_\tau$ [15]. Consequently, this will set the limit on the symbol length that can be used in order to avoid intersymbol interference (ISI). Notice that the delay spread would still be nearly zero as long as the LoS path dominates.

4) Rician Factor K_{rf}: If we keep the assumption of the transmitted power as 1 W valid, the power ratio between the LoS and the NLoS links can be quantified by the Rician factor: $K_{\text{rf}} = \frac{P_{LoS}}{P_{NLoS}}$ [5].
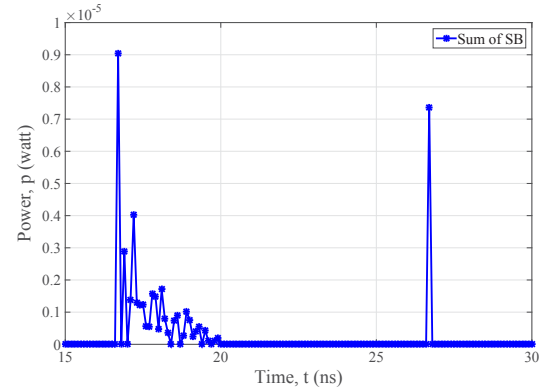
All above fundamental channel characteristics are presented in Table III. In term of channel DC gain, the theoretical total
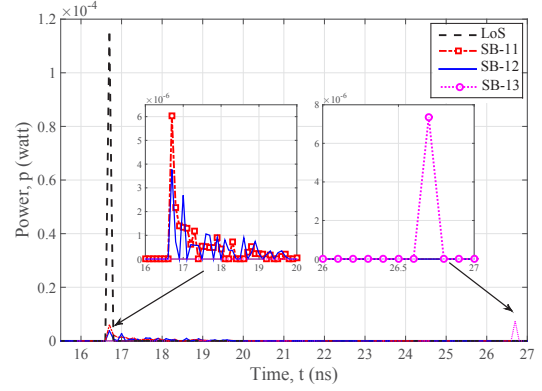
(a) $h_{pq}^{\text{LoS}}(t)$ and $h_{pq}^{\text{SB}}(t)$
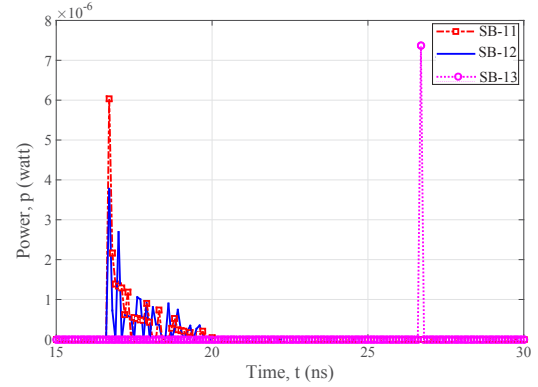
(b) $h_{pq}^{\text{SB}}(t)$

(c) Sum of $h_{pq}^{\text{SB}}(t)$

Fig. 4. VLC CIR (a) LoS and SB, (b) SB, and (c) Sum of SB.

received power is 0.1582 mW. The LoS components carry 0.1146 mW (72.42% of the total received power). While the powers carried by SB_11 and SB_12 components are 12.778 μW and 11.239 μW, respectively, and it is further decrease for SB_13 components to be 7.3638 μW because of the longer path length and larger AoD and/or AoA that ellipse made with the Tx and/or Rx, with respect to the normal on the Tx or Rx planes. Therefore SB components carry 31.38 μW (19.83%). On the other hand, for DB model, the power carried by DB_21

TABLE III: VLC Channel Characteristics.

	LoS	SB_11	SB_12	SB_13	DB_21	DB_22	DB_23	TB_31
Received Power (W)	0.1146e-03	12.778e-06	11.239e-06	7.3638e-06	8.7387-06	1.4423e-06	1.643e-06	4.3894e-07
Mean Access Delay (ns)	16.7	17.129	17.158	26.7	17.743	27.966	29.161	29.722
RMS Delay Spread (ns)	0	0.47092	0.62552	0	0.90587	1.3227	1.8323	1.7832
K_Factor	1	3.6517			9.6914			261.07

(a) $h_{pq}^{\mathrm{DB}}(t)$
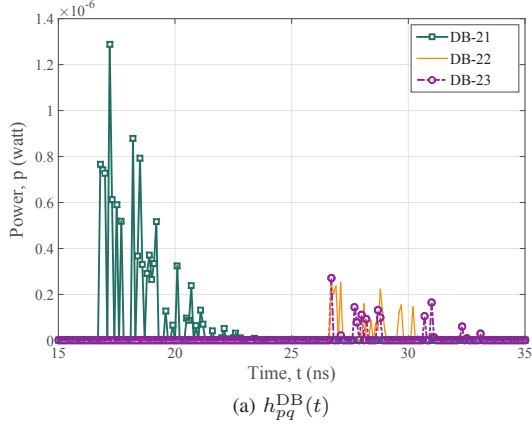
Fig. 6. VLC CIR of TB ($h_{pq}^{\mathrm{TB}}(t)$)
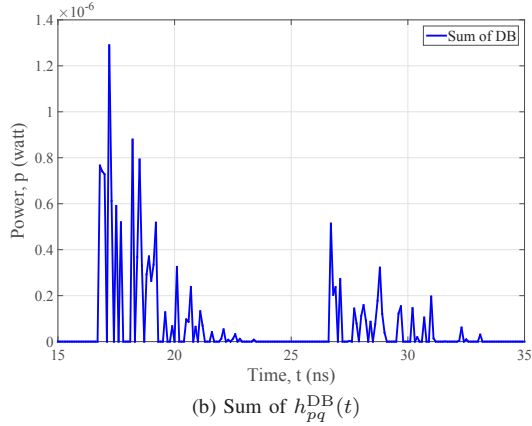
(b) Sum of $h_{pq}^{\mathrm{DB}}(t)$

Fig. 5. VLC CIR (a) DB and (b) Sum of DB.

Fig. 7. Combined CIR of SB, DB, and TB.

components is 8.7387 μW. It can be noted that the powers carried by DB_21 and SB_13 components are close to some extent although DB_21 components have shorter path length and this is due to the higher losses resulting from $\rho_{\mathrm{scaterer}}(\lambda)$ compared with $\rho_{\mathrm{wall}}(\lambda)$. DB_22 and DB_23 components carry 1.4423 μW and 1.643 μW, respectively because of the long path length compared with DB_21. Hence DB components carry 1.1824 μW (7.47%). Finally, the power carried by TB_31 components is no more 0.43894 μW (0.28%) since it is pass longer path length and scattered triple. Fig. 10 illustrates our results compared with the results of [8] up to three bounces. The slight difference is due to that reflectivity values in IR band are larger than those in VL band [10]. Furthermore, we can see after first bounce, the contribution of lower reflectivity of VL band affects received power.

In term of the RMS delay spread, it is obvious that the delay is related to the path length. Furthermore it is worth
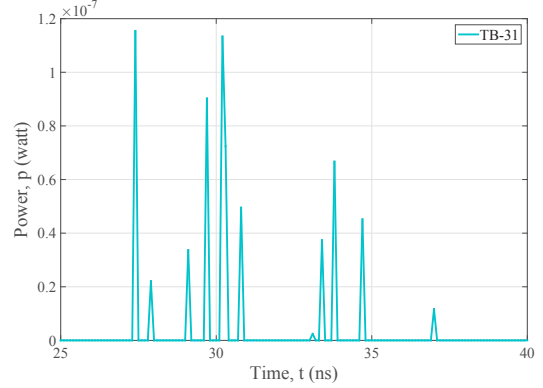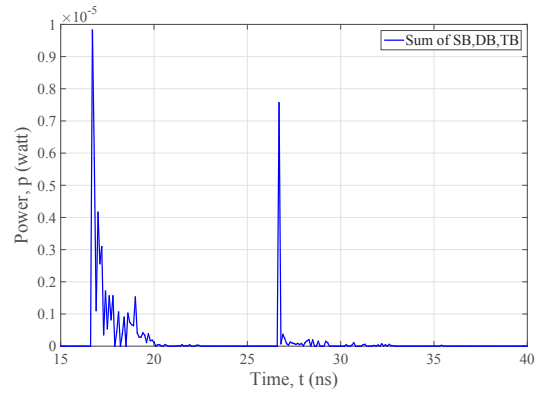
to notice that DB_21 components arrive much earlier than DB_22 and DB_23 components and hence overleaping with SB_11 and SB_12 components. Although, DB_21 carries less power compared with SB_11 and SB_12 as shown in Fig. 8, because they are scattered twice, some component have high power since they have small AoD and/or AoA with respect to the normal on the Tx or Rx planes. Accordingly, this will add a significant amount of power for total power as shown in the sum of CIR in Fig. 7. Also, it is observed that DB_21 components arrive even much earlier than that SB_13 as a result of shorter path length. Finally, TB_31 components arrive later than all previous ones as illustrated in Fig. 6. We can see that TB_31 components are overlapping with DB_22 and DB_23 components as shown in Fig. 9, but have less power since they are scattered triple and have less number of components and this latter can be interpreted as a result of the two practical criteria mentioned above.
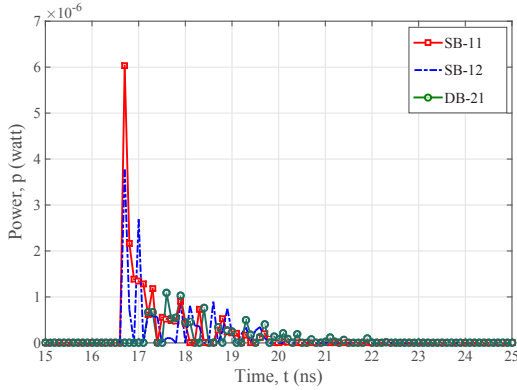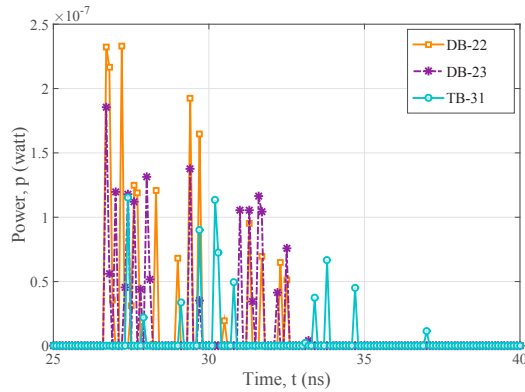
Fig. 8. Overlapping of SB_11, SB_12 and DB_21.

Fig. 9. Overlapping of DB_22, DB_23 and TB_31.

VI. CONCLUSIONS

In this paper, we have proposed a novel RS-GBMB model for VLC channels. Based on the proposed model, geometrical properties have been derived and VLC channel characteristics have thoroughly been investigated. The simulation results have validated the utility of the proposed model compared with the existing models. Our results have demonstrated that the LOS component can carry a significant amount of power compared with the primary reflections (up to 3). However, the primary reflections tend to add to a significant amount as they sum together. VLC channel characteristics of the proposed model such as channel gain, RMS delay spread, and Rician factor have been investigated and analyzed with respect to optical path length, AoD/AoA, and scatterers and their reflection coefficients.
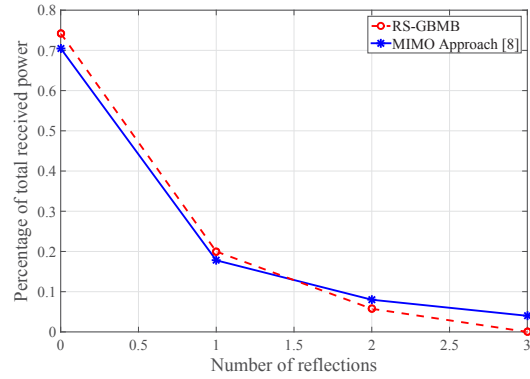
ACKNOWLEDGMENT

Fig. 10. Percentage of received power vs. number of reflections.

REFERENCES

[1] C.-X. Wang, F. Haider, X. Gao, X.-H. You, Y. Yang, D. Yuan, H. Aggoune, H. Haas, S. Fletcher, and E. Hepsaydir, "Cellular architecture and key technologies for 5G wireless communication networks," *IEEE Commun. Mag.*, vol. 52, no. 5, pp. 122–130, Feb. 2014.

[2] H. Haas. (2011, July) *Wireless data from every light bulb* [Online]. Available: http:// www.ted.com.

[3] N. Sklavos, M. Huebner, D. Goehringer, and P. Kitsos, *System-Level Design Methodologies for Telecommunication*, London, UK, Springer, 2014.

[4] V. Dixit, S. Shukla and M. Shukla, "Performance analysis of optical IDMA system for indoor wireless channel model," in *Proc. CICN'12*, Mathura, India, Nov. 2012.

[5] Z. Ghassemlooy, W. Popoola, and S. Rajbhandari, *Optical Wireless Communications: System and Channel Modelling with MATLAB*, 1st ed, CRC press, New York, USA, 2013.

[6] F. R. Gfeller and U. Bapst, "Wireless in-house data communication via diffuse infrared radiation," in *Proc. IEEE*, vol. 67, no. 11, pp. 1474–1486, Nov. 1979.

[7] J. R. Barry, *Wireless Infrared Communications*, Kluwer Academic Publishers, USA, 1994.

[8] Y. A. Alqudah and M. Kavehrad, "MIMO characterization of indoor wireless optical link using a diffuse-transmission configuration," *IEEE Trans. Commun.*, vol. 51, no. 9, pp. 1554–1560, Sept. 2003.

[9] E. Sarbazi, M. Uysal, M. Abdallah, and K. Qaraqe, "Indoor channel modelling and characterization for visible light communications," in *Proc. ICTON'14*, Graz, Austria, July 2014.

[10] F. Miramirkhani, M. Uysal, and E. Panayircib, "Novel channel models for visible light communications," in *Proc. SPIE'15*, San Francisco, USA, Feb. 2015.

[11] DIALux [Online]. Available: http:// www.dial.de/ DIAL/.

[12] X. Cheng, C.-X. Wang, H. Wang, X. Gao, X.-H. You, D. Yuan, B. Ai, Q. Huo, L. Song, and B. Jiao, "Cooperative MIMO channel modeling and multi-link spatial correlation properties," *IEEE JSAC'12*, vol. 30, no. 2, pp. 388–396, Feb. 2012.

[13] X. Cheng, C.-X. Wang, D. I. Laurenson, S. Salous, and A. V. Vasilakos, "An adaptive geometry-based stochastic model for non-isotropic MIMO mobile-to-mobile channels," *IEEE Trans. Wireless Commun.*, vol. 8, no. 9, pp. 4824–4835, Sept. 2009.

[14] E. W. Weisstein, *CRC Concise Encyclopedia of Mathematics*, 2nd ed, CRC press, New York, USA, 2003.

[15] D. Wu, Z. Ghassemlooy, S. Rajbhandari, and H. Le Minh, "Channel characteristics analysis and experimental demonstration of a diffuse cellular indoor visible light communication system," *The Mediterranean Journal of Electronics and Communications*, vol. 8, pp. 1–7, 2012.